The Astrophysical Journal, 942:95 (15pp), 2023 January 10 https://doi.org/10.3847/1538-4357/aca66c

Application of Convolutional Neural Networks to Predict Magnetic Fields' Directions in Turbulent Clouds

Duo Xu[1], Chi-Yan Law[2,3], and Jonathan C. Tan[1,2]
[1] Department of Astronomy, University of Virginia, Charlottesville, VA 22904-4235, USA; xuduo117@virginia.edu
[2] Department of Space, Earth & Environment, Chalmers University of Technology, SE-412 96 Gothenburg, Sweden
[3] European Southern Observatory, Karl-Schwarzschild-Strasse 2, D-85748 Garching, Germany
Received 2022 October 20; revised 2022 November 24; accepted 2022 November 25; published 2023 January 17

Abstract

We adopt the deep learning method CASI-3D (convolutional approach to structure identification-3D) to infer the orientation of magnetic fields in sub-/trans-Alfvénic turbulent clouds from molecular line emission. We carry out magnetohydrodynamic simulations with different magnetic field strengths and use these to generate synthetic observations. We apply the 3D radiation transfer code RADMC-3D to model ^{12}CO and ^{13}CO (J = 1−0) line emission from the simulated clouds and then train a CASI-3D model on these line emission data cubes to predict magnetic field morphology at the pixel level. The trained CASI-3D model is able to infer magnetic field directions with a low error ($\lesssim 10^{\circ}$ for sub-Alfvénic samples and $\lesssim 30^{\circ}$ for trans-Alfvénic samples). We further test the performance of CASI-3D on a real sub-/trans- Alfvénic region in Taurus. The CASI-3D prediction is consistent with the magnetic field direction inferred from Planck dust polarization measurements. We use our developed methods to produce a new magnetic field map of Taurus that has a three times higher angular resolution than the Planck map.

Unified Astronomy Thesaurus concepts: Interstellar medium (847); Interstellar magnetic fields (845); Convolutional neural networks (1938); Molecular clouds (1072); Magnetohydrodynamics (1964)

1. Introduction

Magnetic (*B*-) fields are ubiquitous in the universe (e.g., Crutcher 1999; Han 2017). They are one of the major components regulating the motion and evolution of the interstellar medium (ISM; Crutcher 2012; Federrath 2015). Although gravity and turbulence also play important roles in the formation of structures in the ISM (Padoan & Nordlund 1999; Elmegreen & Scalo 2004; McKee & Ostriker 2007), recent studies indicate that magnetic fields are also very important over a wide range of regimes and scales (Li et al. 2009; Clark et al. 2014; Zhang et al. 2019). However, measuring *B* fields is challenging. The observations of magnetic fields are divided into two main types of measurement. One is the plane-of-sky (POS) component, which is usually traced by polarized thermal dust emission (Rao et al. 1998; Planck Collaboration et al. 2016), starlight polarization (Davis & Greenstein 1951; Fosalba et al. 2002), and synchrotron emission (Beck & Graeve 1982; Jansson & Farrar 2012). The other is the line-of-sight (LOS) component, which is normally resolved by Zeeman splitting (Troland & Heiles 1986; Crutcher et al. 2010) and Faraday rotation (Burn 1966; Hutschenreuter et al. 2022).

Although we have multiple approaches to trace POS *B* fields, their study remains challenging. For example, starlight polarization is limited by the lines of sight along which stars are present and detectable. The polarized thermal dust emission is considered to be caused by radiative torques (RATs) produced by anisotropic radiation flux with respect to the magnetic field (Hoang & Lazarian 2008), which imposes other conditions related to the presence of such flux. Moreover, both methods only trace the projected POS magnetic field direction and are not capable of distinguishing the POS *B* fields for different gas components on the LOS.

Approaches to studying *B* fields based on theories of interstellar magnetohydrodynamic (MHD) turbulence and turbulent reconnection have also been developed (Goldreich & Sridhar 1995; Lazarian & Vishniac 1999). Goldreich & Sridhar (1995) examined the effects of the interaction among shear Alfvén waves and found that turbulent eddies become elongated along the magnetic field direction in the limit of strong Alfvén turbulence, where the perturbed velocity is much smaller than the Alfvén velocity, i.e., sub-Alfvénic. Based on this crucial principle, a method to trace the direction of magnetic fields by using spectroscopic data has been developed, i.e., the velocity channel gradient technique (VGT[4], Lazarian & Yuen 2018; Heyer et al. 2020). VGT examines maps of line emission from the gas in small velocity ranges and measures the gradient in intensity of this emission in small patches, i.e., "subblocks." Then the plane of the sky magnetic field direction is assumed to be in the direction perpendicular to this gradient.

VGT has been examined in numerical simulations and synthetic spectroscopic data (Yuen & Lazarian 2017; Lazarian & Yuen 2018) and tested on observational data (Hu et al. 2019; Liu et al. 2022). However, Yuen & Lazarian (2017) pointed out that the gradient calculation requires subblock averaging to obtain a robust result and this averaging process limits the

[4] There are different acronyms or naming of the same technique in different literature studies, including velocity channel gradient (VchG) in Lazarian & Yuen (2018) and "gradients of surface brightness within thin velocity slices" in Heyer et al. (2020). Also, the original velocity gradient technique (González-Casanova & Lazarian 2017) was applied on the velocity centroid map instead of thin-slice velocity channel maps. Here we will use the acronym VGT throughout the work to preserve the original spirit of using velocity gradients as a means of magnetic field tracing.

Table 1
Physical Properties of the Simulations[a]

Model	$\alpha_{\rm vir}$	$\mathcal{M}_A$	$\mu_{\rm Phi}$	$N_{\rm seed}$
Turb1	1	1.24	2	2
Turb2	1	0.62	1	2
Turb3	2	1.75	2	2
Turb4	2	0.87	1	2

Note.
[a] Model name, virial parameters, Alfvén mach number, mass-to-flux ratio, and the number of different turbulent driving patterns.

resolution that can be achieved to determine *B*-field morphology. Furthermore, it remains somewhat unclear about the accuracy of the VGT method in different situations of application. For example, Clark et al. (2019) pointed out that the gas emission in the velocity channel maps, such as the H I 21 cm line, is not dominated by velocity fluctuations, but rather by density fluctuations, which implies that the fundamental assumption of VGT is not valid any more. In addition, when self-gravity is important, then the velocity structures will be influenced by additional effects that would lead to VGT analysis yielding inaccurate results (e.g., Luk et al. 2022). Nevertheless, while the importance of velocity fluctuations on the gas emission in thin velocity channels is still under debate, a number of simulations have demonstrated that magnetic fields can play an important role in shaping the morphology of gas emission in velocity channel maps (Soler et al. 2013; Inoue & Inutsuka 2016; Soler & Hennebelle 2017). Moreover, an increasing amount of observational evidence shows that the morphology of the ISM is regulated by magnetic fields, including the atomic cold neutral medium (Clark et al. 2014, 2015) and molecular gas (Soler 2019; Heyer et al. 2020), including via polarized dust emission (Soler et al. 2017). Consequently, we introduce a deep learning method, i.e., via convolutional neural networks (CNNs), to examine the morphology of spectroscopic data and infer the magnetic field directions in simulations and observations of the ISM.

CNNs have gained increasing popularity among astronomers and are widely used for a variety of tasks, including galaxy morphology prediction (Dieleman et al. 2015), exoplanet detection (Pearson et al. 2018), and stellar feedback bubble identification (Van Oort et al. 2019). CNNs learn the morphology and extract the feature of objects by applying a series of kernels to convolve with the input data. CNNs are proficient at identifying and outlining objects from the input data. Xu et al. (2020a, 2020b) developed a convolutional approach to structure identification-3D (CASI-3D) based on CASI-2D (Van Oort et al. 2019) to identify stellar feedback bubbles and protostellar outflows in position-position–velocity (PPV) molecular line spectral cubes. Xu et al. (2020a, 2020b) trained CASI-3D on synthetic molecular line spectral cubes and applied it to real observations. They identified all previously visually identified feedback structures in nearby molecular clouds (Xu et al. 2022). Bai et al. (2021) applied CNNs to infer the radial component and the transverse magnetic field of the Sun from 2D photospheric continuum images and achieved a low uncertainty ∼10%. This demonstrates the ability of CNNs to infer magnetic fields based on the morphology of emission and/or absorption. Peek & Burkhart (2019) applied CNNs to distinguish between sub-Alfvénic and super-Alfvénic turbulence from the Fourier phase space of a density slice from simulations and achieved a high accuracy >98%. This work indicates that there is a significant amount of information in images, e.g., in Fourier phase space, compared to just a single power spectrum. The results from Peek & Burkhart (2019) and Bai et al. (2021) indicate that CNNs are able to retrieve more information, e.g., magnetic fields information at the pixel level, from PPV cubes.

In this paper, we adopt the deep learning method CASI-3D to infer the orientation of magnetic fields in sub-/trans-Alfvénic turbulent clouds from molecular line emission. We describe CASI-3D and how we generate the training set from synthetic observations in Section 2. Here we also introduce the CO observations and Planck dust polarization data. In Section 3, we evaluate our CNN models in predicting the orientation of magnetic fields on synthetic observations and present the performance of CNN models on real observations. We summarize our results and conclusions in Section 4.

2. Data and Method

2.1. Magnetohydrodynamics Simulations

We conduct ideal MHD simulations with ORION2 (Li et al. 2012) to model sub- and trans-Alfvénic turbulent clouds. The simulation box is $5 \times 5 \times 5$ pc^3 with periodic boundary conditions and without self-gravity. The magnetic field is initialized along the *z*-direction. We treat the gas as an isothermal ideal gas with an initial cloud temperature of 10 K. The three-dimensional Mach number is 10.5, which places the simulated cloud on the line width–size relation, $\sigma_{\rm 1D} = 0.72 R_{\rm pc}^{0.5}$ km s^{-1} (McKee & Ostriker 2007). The calculations use a base grid of 256^3. We conduct simulations with two sets of virial parameters $\alpha_{\rm vir} = 5\sigma_v^2 R/(GM)$: $\alpha_{\rm vir} = 1$, which corresponds to a mean H-nuclei density of $n_{\rm H} = 1046$ cm^{-3} and total mass of 3767 $M_\odot$, and $\alpha_{\rm vir} = 2$, which corresponds to a mean H-nuclei density of $n_{\rm H} = 523$ cm^{-3} and total mass of 1884 $M_\odot$. Furthermore, for each value of $\alpha_{\rm vir}$ we run two sets of simulations with different mass-to-flux ratios $\mu_\Phi = M_{\rm gas}/M_\Phi = 2\pi G^{1/2} M_{\rm gas}/({\rm BL}^2)$, $\mu_\Phi = 1$ and 2, which yields an Alfvén mach number between 0.6 and 1.7, indicating a sub-/trans-Alfvénic turbulent cloud. We initialize the density and velocity fields by driving the simulation gas for two Mach crossing times without gravity, but adding random large-scale perturbations with Fourier modes $1 \leqslant k \leqslant 2$ (Mac Low 1999). We list the physical properties of the simulations in Table 1.

2.2. Training Sets

We apply the publicly available radiative transfer code RADMC-3D (Dullemond et al. 2012) to model ^{12}CO ($J = 1 - 0$) and ^{13}CO ($J = 1 - 0$) line emission of the turbulent clouds. We adopt the simulation density, temperature, and velocity distributions as the RADMC-3D inputs. In the radiative transfer, we assume that H_2 is the only collisional partner of CO. We take 62 as the fiducial abundance ratio between ^{12}CO and ^{13}CO and 10^{-4} as the abundance ratio between ^{12}CO and H_2.

Figure 1 shows the synthetic ^{13}CO (1−0) integrated intensity and the POS magnetic field direction of the MHD simulation with different Alfvén mach numbers. Since the magnetic fields are initialized along the *z*-axis in these MHD simulations, the POS magnetic field directions viewed along the *z*-axis are less ordered. To reduce the impact of the turbulence dominant pattern rather than that regulated by magnetic fields, we rotate the turbulent box following Euler angles (α, β, γ) and conduct

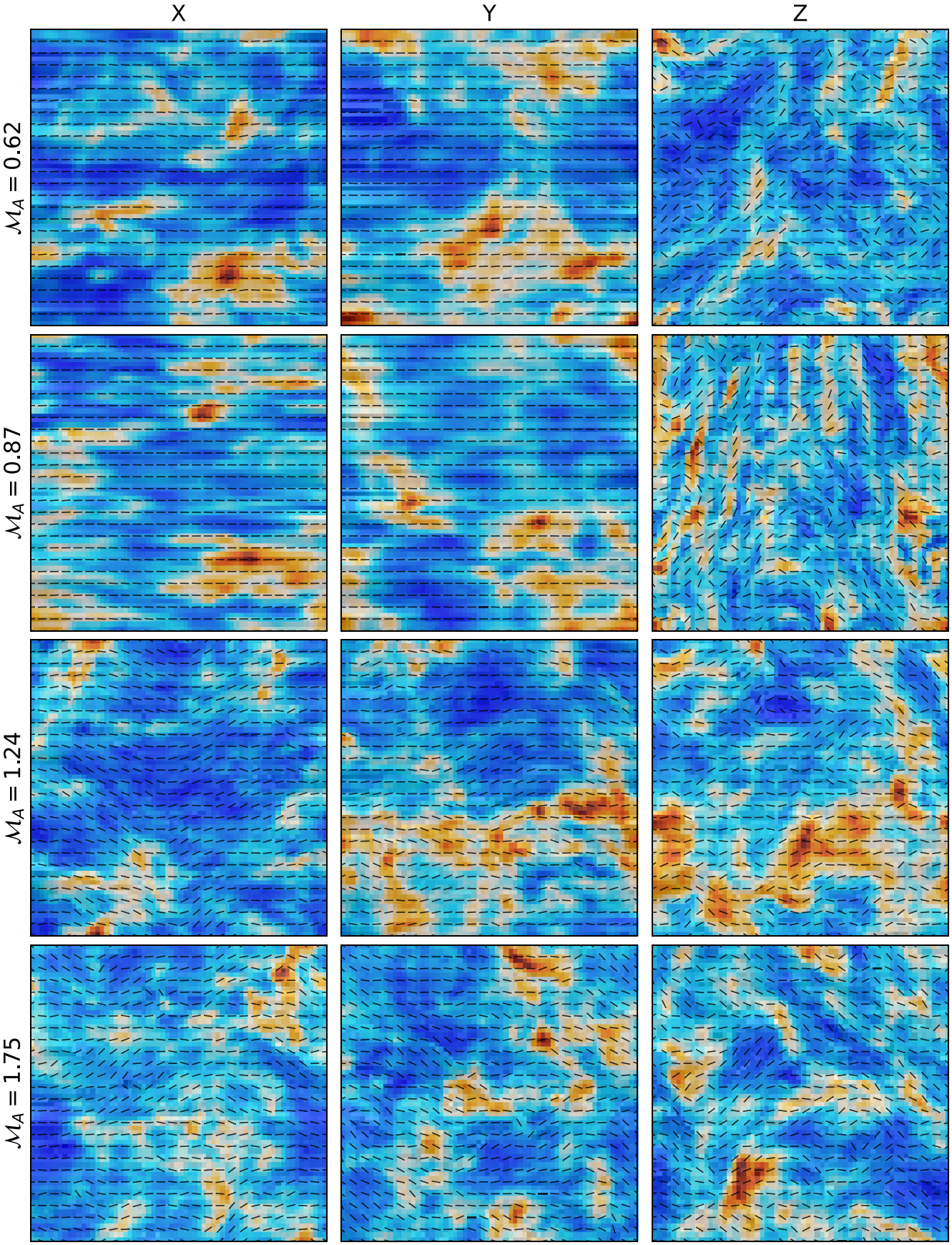

Figure 1. Synthetic ^{13}CO (1−0) integrated intensity overlaid with the direction of magnetic fields. Three columns are three different viewing directions. Four rows represent simulations with different Alfvén mach numbers, as labeled.

the radiative transfer from the new axes. We choose three sets of Euler angles (15°, 15°, 15°), (30°, 30°, 30°), and (45°, 45°, 45°). Figure 2 shows the synthetic ^{13}CO integrated intensity and the POS magnetic fields directions of the MHD simulations rotated by Euler angles of (45°, 45°, 45°).

To enhance the diversity of physical and chemical conditions for the training set, we generate synthetic observations where both ^{12}CO and ^{13}CO abundances are reduced by a factor of 10. We also increase the training set by considering thin clouds with thicknesses between 0.7 and 5 pc using the same method in Xu et al. (2020a). We also conduct synthetic observations with different physical scales, i.e., a "zoomed-in" synthetic observation with an image size of 2.5 pc × 2.5 pc, and 1.25 pc × 1.25 pc, and a zoomed-out synthetic observation with an image size of 5 pc × 5 pc. In addition to the different image sizes, we resample the synthetic observations with two different velocity resolutions: at low resolution with an interval of 0.25 km s^{-1}; and at high resolution with an interval of 0.125 km s^{-1}. Additionally, we rotate the images randomly from 0° to 360° and randomly shift the central velocity of the cubes from −3 to +3 km s^{-1}. Considering the optically thick emission of ^{12}CO, we adopt ^{13}CO emission as the training set for CASI-3D, which better outlines the morphology of the clouds. It is worth noting that the CASI-3D model cares about the relative intensity of the data cube and does not require the data cube from a specific molecule. It is able to handle spectroscopic data from different molecules or atoms.

We then derive the magnetic field directions of the gas at each velocity channel from the simulation data. We first bin the LOS gas into velocity channels and calculate the mass-weighted magnetic field direction in each channel. The input data for CASI-3D model is the PPV ^{13}CO data cube, and the target is the corresponding PPV magnetic field directions. In total we generate 11,540 synthetic cubes: 6924 as a training set, 2308 as a test set, and 2308 as a validation set.

2.3. CASI-3D: Inferring Orientation of Magnetic Fields

In this section, we introduce a new CASI-3D model to predict the orientation of magnetic fields from molecular line emission. We adopt the same CNN architecture, CASI-3D, from Xu et al. (2020a). CASI-3D is an autoencoder with both residual networks (He et al. 2016) and a "U-net" (Ronneberger et al. 2015). We adopt the same hyperparameters as Xu et al. (2020a, 2020b).

2.4. Observations

2.4.1. ^{12}CO and ^{13}CO Data

The ^{12}CO ($J = 1 - 0$) and ^{13}CO ($J = 1 - 0$) lines were observed simultaneously in surveys of Taurus between 2002 and 2005 using the 13.7 m Five College Radio Astronomy Observatory (FCRAO) Telescope (Narayanan et al. 2008). The ^{12}CO and ^{13}CO maps are centered at $\alpha(2000.0) = 04^{\rm h}32^{\rm m}44\overset{\rm s}{.}6$, $\delta(2000.0) = 24°25'13\overset{''}{.}08$ covering an area of 98 deg^2. The main beam of the antenna pattern has an FWHM of 45″ for ^{12}CO and 47″ for ^{13}CO. The data are obtained on the fly, but they are resampled onto a uniform 23″ grid (Ridge et al. 2006). The Taurus data has an rms antenna temperature of 0.28 K for ^{12}CO and 0.125 K for ^{13}CO. There are 80 and 76 channels with 0.26 and 0.27 km s^{-1} spacing for ^{12}CO and ^{13}CO, respectively. The velocity range of the Taurus data spans −5.1–14.9 km s^{-1}.

2.4.2. Planck 353 GH Dust Polarization Map

We adopt the data from the Planck 3rd Public Data Release (Planck Collaboration et al. 2020). We infer the magnetic field orientation from the dust polarization angle:

$$\phi_B = \frac{1}{2}\arctan 2(-U, Q) + \frac{\pi}{2}, \quad (1)$$

where Q and U are the Stokes parameters of polarized dust emission, and arctan 2 is the two arguments arctangent function that returns the angle in the range (-π,π). The maps of Q and U are initially at 4′ 8 resolution in HEALPix format with an effective pixel size of 1′ 07.

3. Results

3.1. Evaluation of CASI-3D Performance on Synthetic Observations

In this section, we use the synthetic data to assess how accurately magnetic field orientations can be determined from molecular line emission.

We evaluate the performance on the test samples with different Alfvén mach numbers that are not included in the training set. Figure 3 shows the performance of CASI-3D to infer the orientation of magnetic fields on four clouds with different Alfvén mach numbers. The "true" magnetic field directions are derived by a mass-weighted averaging of the POS magnetic field direction along each LOS. It is worth noting that CASI-3D predicts the POS magnetic field direction at each velocity channel. We average the CASI-3D predicted POS magnetic field on each LOS by emission intensity weighting.

In addition, we evaluate the POS magnetic field direction calculated from the VGT method. We follow the same strategy in Soler et al. (2019) and Heyer et al. (2020) to calculate the gradient of the intensity of each velocity channel. The magnetic field direction is estimated here as the angle of the vector normal to the gradient vector, i.e., $\Phi_{\rm B,VGT} = \Phi_{\rm Gradient} + \frac{\pi}{2}$. Similarly, we average the VGT predicted POS magnetic field on each LOS by emission intensity weighting. As discussed in Luk et al. (2022), the VGT inferred POS magnetic field direction might be significantly different depending on the choice of velocity range. To make fair comparison in this work, we do not choose specific velocity ranges, but include all channels for the result from VGT and CASI-3D.

As shown in Figure 3, CASI-3D is able to predict the magnetic field orientation with high accuracy in sub-Alfvénic clouds. When the magnetic field becomes weaker, the cloud transitions to being trans-Alfvénic, where turbulence plays a more significant role in modifying the morphology of the cloud as well as the magnetic field lines. Although CASI-3D is still able to correctly infer roughly half of the magnetic field direction in trans-Alfvénic clouds, it fails at some places where magnetic fields are not the major factor regulating the morphology of the cloud. On the other hand, VGT predicts the magnetic field directions with a lower accuracy, even in sub-Alfvénic clouds. VGT is likely sensitive to the local intensity fluctuations, which might not truly catch the larger scale morphology. This is the reason why VGT requires large block smoothing on the intensity before calculating, which yields a much lower resolution than that from machine-learning approaches.

To better visualize the prediction of a full PPV cube, we show the channel-by-channel prediction by CASI-3D on a trans-

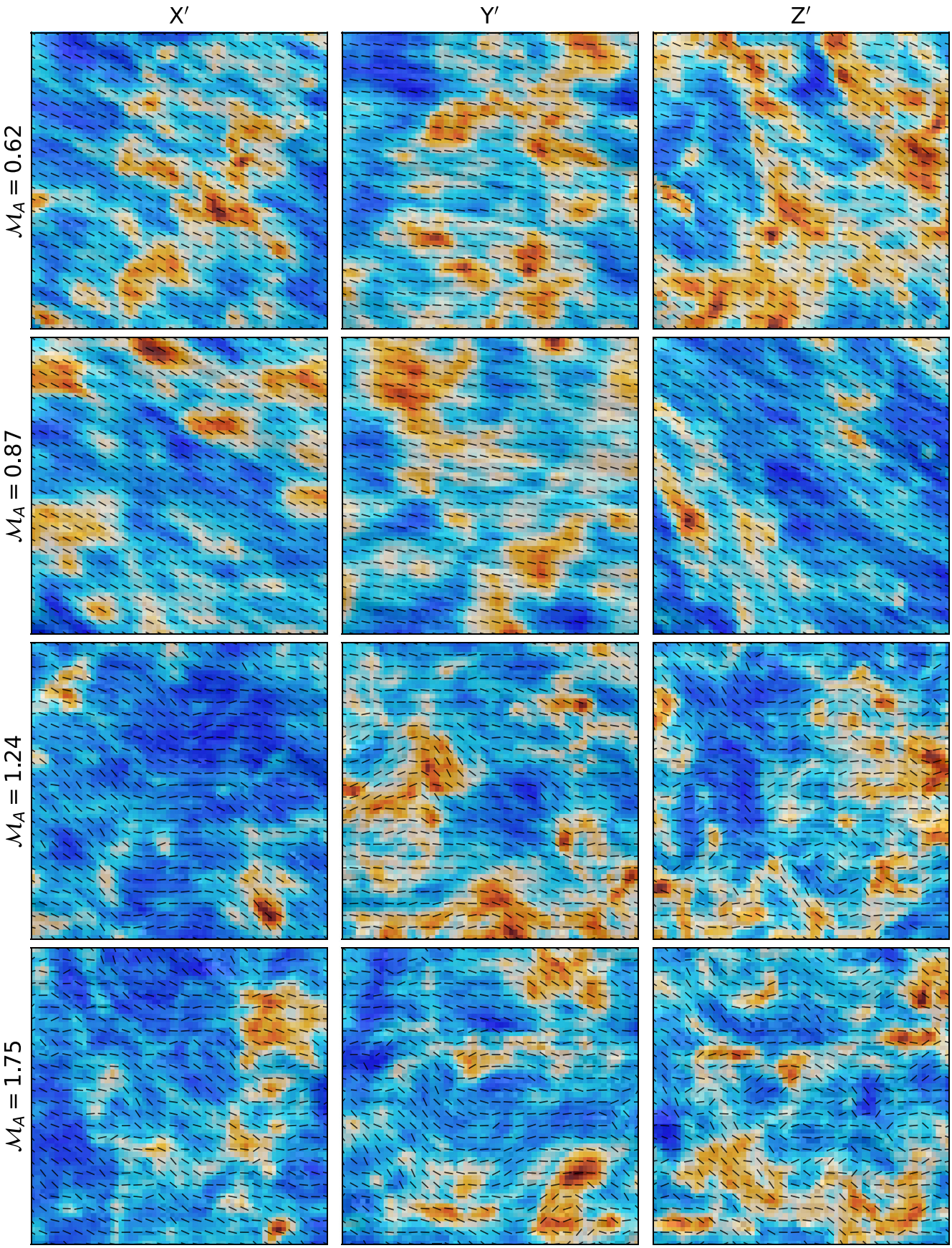

Figure 2. Same as Figure 1, but on a rotated simulation with Euler angles of (45°, 45°, 45°).

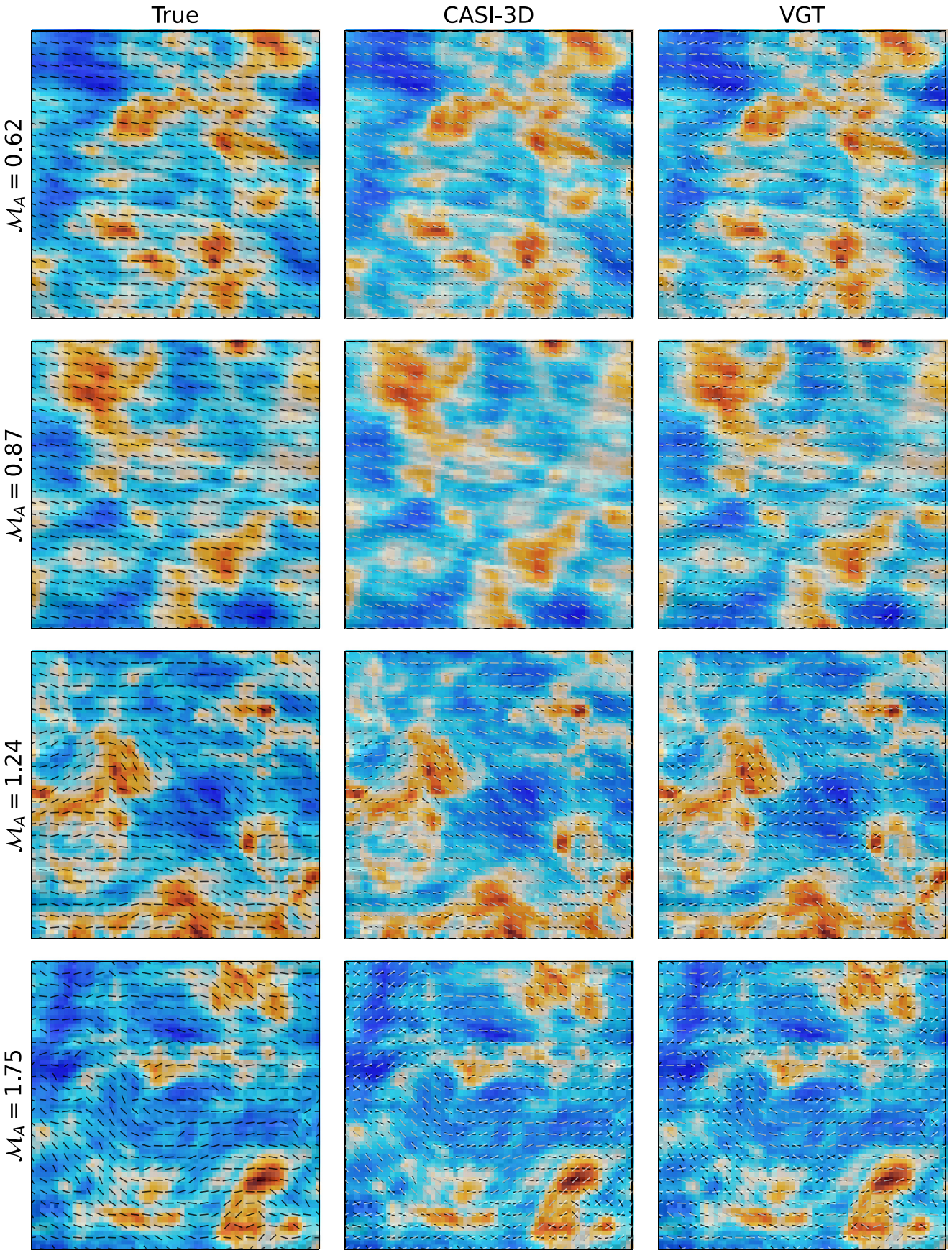

Figure 3. Performance of CASI-3D and VGT to infer the orientation of magnetic fields of four clouds with different Alfvén mach numbers. The background is the integrated ^{13}CO emission. The black lines indicate the true POS magnetic field directions derived from simulations. The gray lines in the middle column indicate the POS magnetic field directions predicted by CASI-3D. The gray lines in the right column indicate the POS magnetic field directions calculated by VGT.

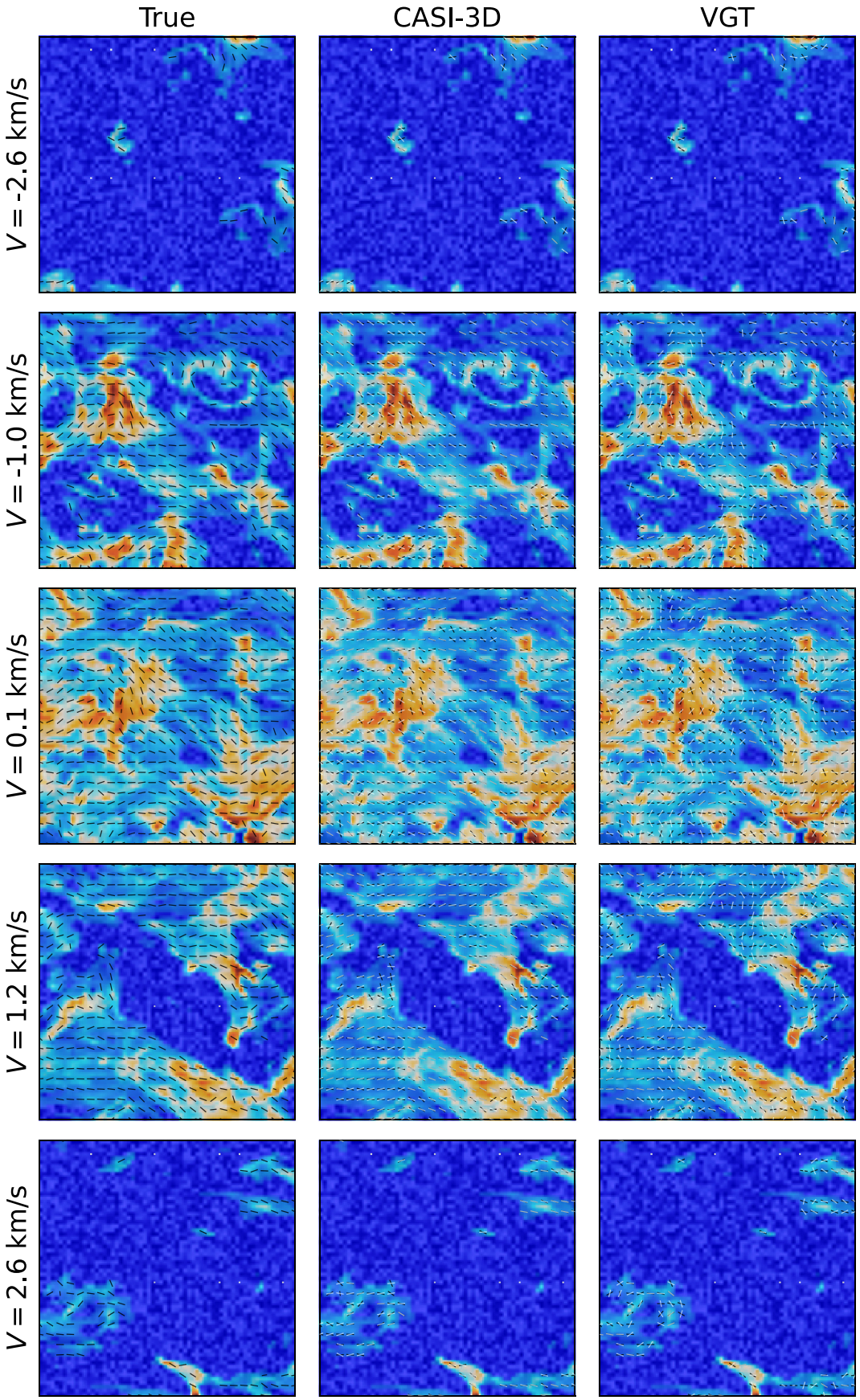

Figure 4. Performance of CASI-3D and VGT to infer the orientation of magnetic fields across multiple velocity channels on a trans-Alfvénic cloud with $\mathcal{M}_A = 1.24$. The background is the ^{13}CO emission at each velocity channel. The black lines indicate the true POS magnetic field directions at each velocity channel. The gray lines in the middle column indicate the POS magnetic field directions predicted by CASI-3D. The gray lines in the right column indicate the POS magnetic field directions calculated by VGT.

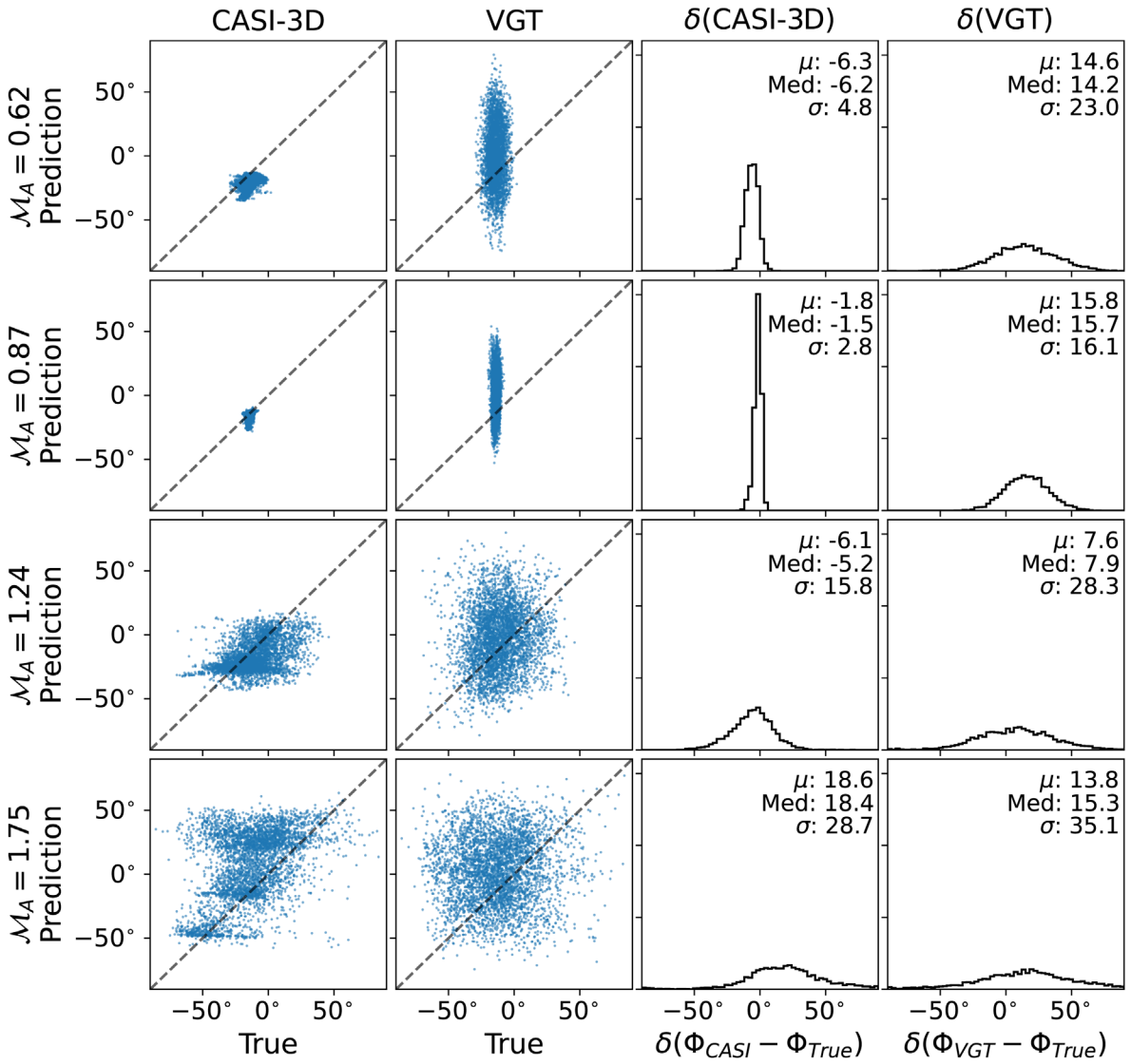

Figure 5. First column: scatter plots between the true magnetic field directions $\Phi_{\rm True}$ and the CASI-3D predicted directions $\Phi_{\rm CASI}$ for the four clouds with different Alfvén mach numbers, as labeled in each row. Second column: scatter plots between the true magnetic field directions $\Phi_{\rm True}$ and the velocity channel gradient (VGT) predicted directions $\Phi_{\rm VGT}$. Third column: histogram of the angle difference between $\Phi_{\rm True}$ and $\Phi_{\rm CASI}$. Fourth column: histogram of the angle difference between $\Phi_{\rm True}$ and $\Phi_{\rm VGT}$.

Alfvénic cloud with $\mathcal{M}_A = 1.24$ in Figure 4. It is obvious that even at the same location the magnetic field direction can be different at different velocities. Neither CASI-3D nor VGT is able to perfectly infer the magnetic field direction at each velocity. However, it is noticeable that CASI-3D prediction has more agreement with the true direction than that of VGT, indicating better performance of CASI-3D than VGT.

To quantify the performances of CASI-3D and VGT, in Figure 5 we present scatter plots between the true magnetic field directions ($\Phi_{\rm True}$) and the predicted ones by CASI-3D ($\Phi_{\rm CASI}$) and by VGT ($\Phi_{\rm VGT}$). The scatter between $\Phi_{\rm True}$ and $\Phi_{\rm CASI}$ is smaller and closer to the one-to-one line than that between $\Phi_{\rm True}$ and $\Phi_{\rm VGT}$. We also show the histogram of the angle difference between $\Phi_{\rm True}$ and $\Phi_{\rm CASI}$, denoted as $\delta_{\rm CASI-3D}$, and also the histogram of the angle difference between $\Phi_{\rm True}$ and $\Phi_{\rm VGT}$, denoted as $\delta_{\rm VGT}$. It is obvious that $\delta_{\rm CASI-3D}$ has a smaller dispersion than $\delta_{\rm VGT}$ for all different Alfvén mach numbers. The dispersion of $\delta_{\rm CASI-3D}$ is the smallest for sub-Alfvénic regions, but becomes larger for trans-Alfvénic regions. We summarize the statistical results in Table 2.

We further examine the performance of CASI-3D on synthetic observations of other simulations (Cho & Lazarian 2003; Burkhart et al. 2009) run by a different code (Cho & Lazarian 2002) in the Appendix. We find that CASI-3D is able to robustly predict magnetic field directions across different sub-Alfvénic simulations with low uncertainties ($\lesssim 15°$).

3.2. CASI-3D Performance on a Trans-Alfvénic Region in Taurus

In this section, we evaluate the CASI-3D performance in the analysis of observational data by comparing the CASI-3D prediction with the dust polarization predicted magnetic field direction. As we discussed above, our CASI-3D model is mainly trained on sub- and trans-Alfvénic clouds. Consequently, we aim to find a sub- and trans-Alfvénic region with molecular line emission data as our test sample. The Taurus striations, which were first presented by Goldsmith et al. (2008) and discussed

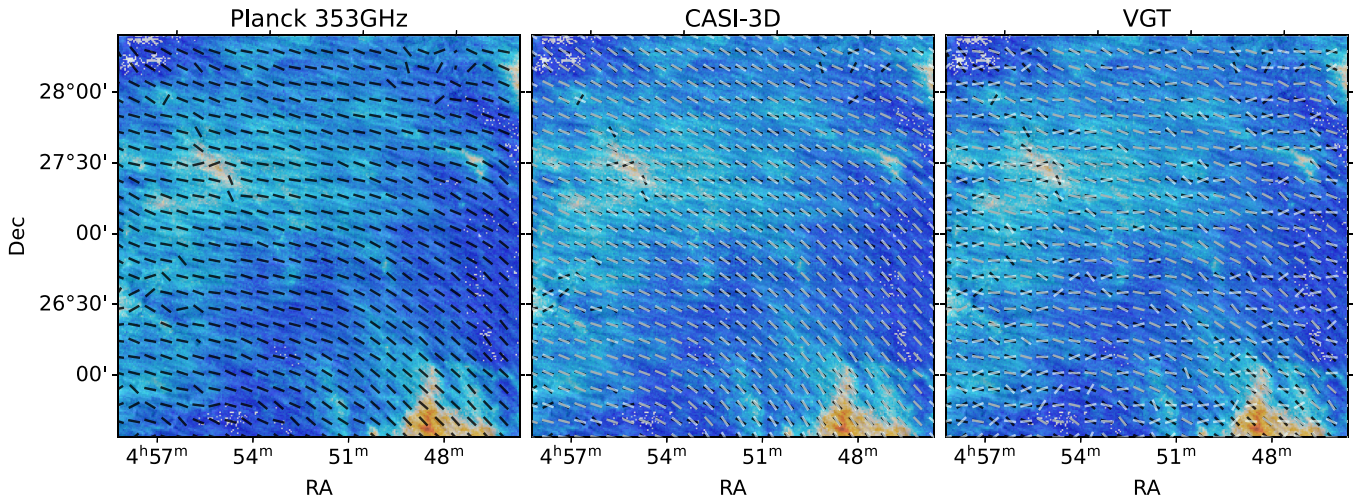

Figure 6. Performance of CASI-3D and VGT to infer the orientation of magnetic fields of the sub-Alfvénic region in Taurus. The background is the integrated ^{12}CO emission. The black lines indicate the POS magnetic field directions calculated from Planck dust polarized emission. The gray lines in the middle column indicate the POS magnetic field directions predicted by CASI-3D. The gray lines in the right column indicate the POS magnetic field directions calculated by VGT.

by Heyer et al. (2016), are likely sub-Alfvénic. Heyer et al. (2016) proposed that the striations are caused by either the Kelvin–Helmholtz instability or magnetosonic waves propagating, both of which are common in sub-Alfvénic clouds.

Figure 6 shows the ^{12}CO integrated intensity of the Taurus striations. We downsample the ^{12}CO data by a factor of 3 to match the pixel resolution of Planck. We also show the magnetic field orientation inferred from Planck dust polarization in Figure 6. We apply the CASI-3D model to the ^{12}CO cube of this sub-Alfvénic region as described in Section 2.4.1. We show the integrated CASI-3D prediction that is averaged over each line of sight by emission weighting in Figure 6. We also show the predicted magnetic field directions by VGT in Figure 6.

It is clear that the CASI-3D prediction agrees with the dust polarization inferred magnetic direction at most locations. There are some localized regions of misalignment where the dust polarization inferred magnetic direction changes significantly. CASI-3D is not sensitive to these small scale fluctuations. CASI-3D predicts the magnetic field direction of each pixel by learning the morphology from it and its surroundings. Consequently, CASI-3D tends to predict a smoother magnetic field direction without sharp fluctuations, which is a limitation of this machine-learning method. On the other hand, the prediction by VGT has a larger deviation from the dust polarization inferred magnetic direction.

To quantify the performance of CASI-3D and that of VGT, in Figure 7 we present scatter plots between the dust polarization inferred magnetic direction $\Phi_{\rm Planck}$ and the predicted ones by CASI-3D $\Phi_{\rm CASI}$, and by VGT $\Phi_{\rm VGT}$. It is clear that the scatter between $\Phi_{\rm Planck}$ and $\Phi_{\rm CASI}$ is closer to the one-to-one line than that between $\Phi_{\rm Planck}$ and $\Phi_{\rm VGT}$. We show the histogram of the angle difference between $\Phi_{\rm Planck}$ and $\Phi_{\rm CASI}$, denoted as $\delta_{\rm CASI-Planck}$, and also the angle difference between $\Phi_{\rm Planck}$ and $\Phi_{\rm VGT}$, denoted as $\delta_{\rm VGT-Planck}$. It is clear that CASI-3D prediction is closer to the dust polarization inferred magnetic direction. The dispersion of $\delta_{\rm CASI-Planck}$ is 9.°5, which is much smaller than the dispersion of $\delta_{\rm VGT-Planck}$, which is 28.°5.

It is worth noting that there are effects that can lead to $\Phi_{\rm Planck}$ yielding an inaccurate estimate of magnetic field direction in CO-emitting molecular gas due to the contaminating effects of polarized dust emission from atomic regions or "CO-dark"

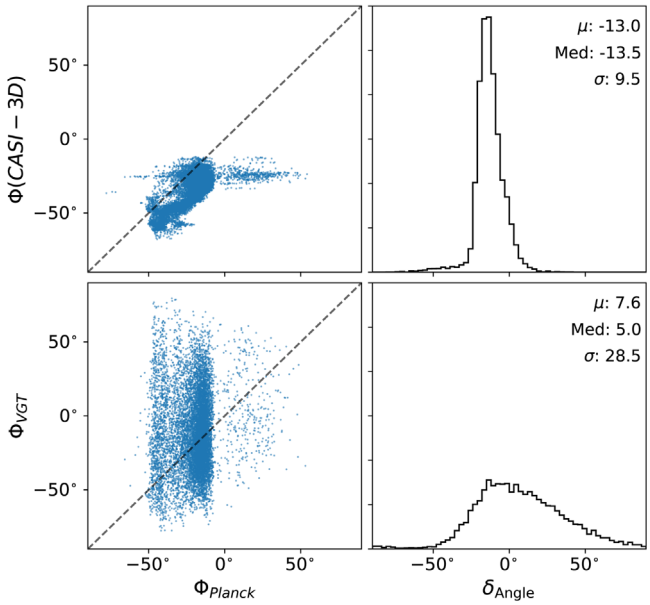

Figure 7. Upper left: scatter plot between the Planck dust polarization inferred magnetic field directions $\Phi_{\rm Planck}$ and the CASI-3D predicted directions $\Phi_{\rm CASI}$ for the sub-Alfvénic region in Taurus. Lower left: scatter plot between the Planck dust polarization inferred magnetic field directions $\Phi_{\rm Planck}$ and the VGT predicted directions $\Phi_{\rm VGT}$. Upper right: histogram of the angle difference between $\Phi_{\rm Planck}$ and $\Phi_{\rm CASI}$. Lower right: histogram of the angle difference between $\Phi_{\rm Planck}$ and $\Phi_{\rm VGT}$.

molecular regions along the LOS. It has long been known that such regions contain dust. For example, Joncas et al. (1992) found spatial correlations between H I emission and infrared circus in filamentary clouds. Planck Collaboration et al. (2011) carried out a more systematic study on the correlation between dust emission and H I emission over 800 deg^2 at high Galactic latitudes, and found that dust emission at lower column densities ($\leqslant 2\times10^{20}$ cm^{-2}) is well correlated with H I emission. This indicates that in such diffuse regions the hydrogen is predominantly in the neutral atomic phase where ^{12}CO is absent, but dust still exists. Moreover, it is also known that there are significant amounts of molecular gas that are dark in ^{12}CO emission (Grenier et al. 2005; Xu et al. 2016) due to

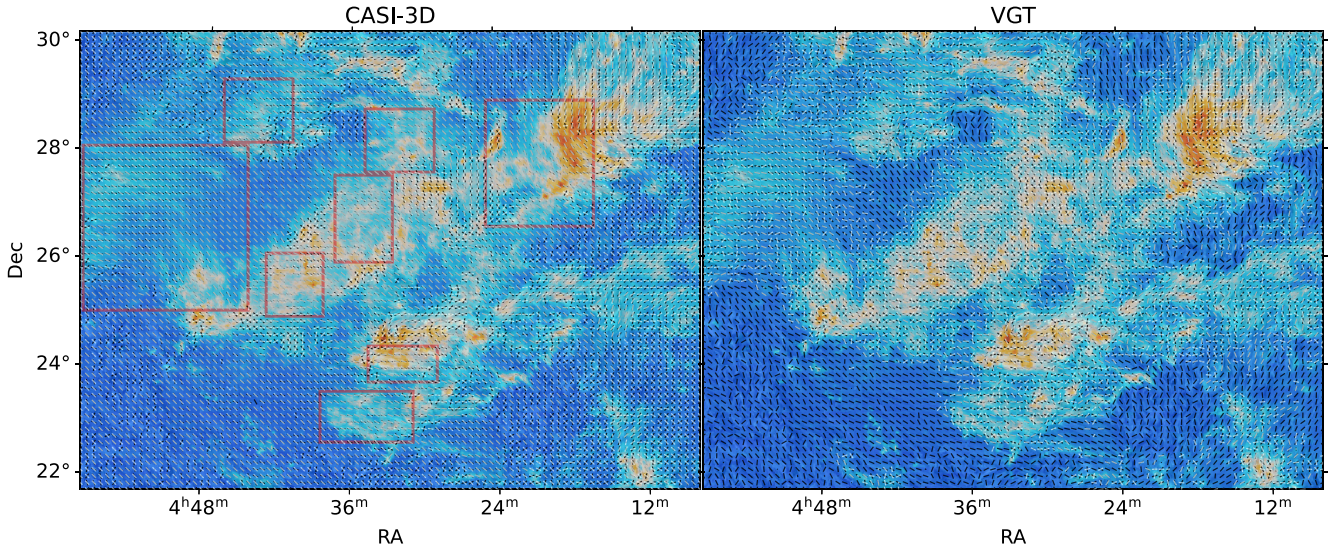

Figure 8. Performance of CASI-3D and VGT to infer the orientation of magnetic fields of the full Taurus map. The background is the integrated ^{12}CO emission. The black lines indicate the POS magnetic field directions calculated from Planck dust polarized emission. The gray lines in the left panel indicate the POS magnetic field directions predicted by CASI-3D. The gray lines in the right panel indicate the POS magnetic field directions calculated by VGT. The red boxes highlight some regions, where CASI-3D inferred magnetic field direction is similar to that by Planck dust polarized emission.

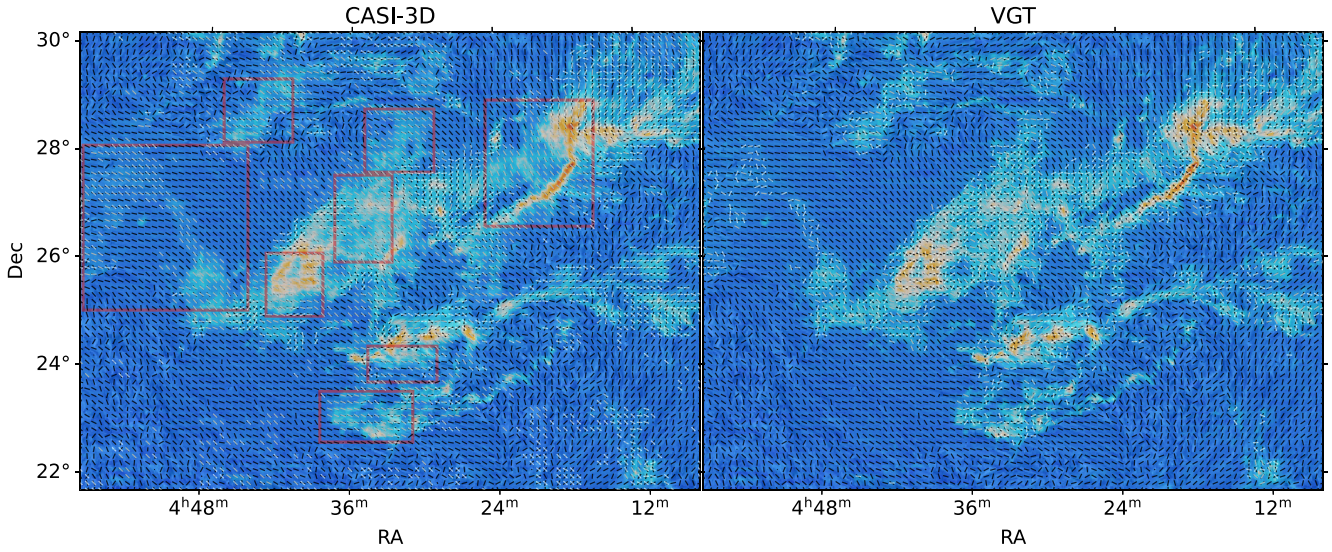

Figure 9. Same as Figure 8, but for ^{13}CO.

photodissociation of CO (e.g., Hollenbach & Tielens 1999) or destruction by cosmic rays (e.g., Bisbas et al. 2015, 2021). Xu et al. (2016) found that the dark molecular gas fraction can be up to 80% at $A_V \sim 1$ mag in local Galactic clouds. Thus, perfect agreement between dust polarization based and ^{12}CO based *B*-field measurements is not expected in general due to LOS dust contamination. This effect could help explain the systematic offset of about $-13°$ that is seen between $\Phi_{\rm CASI}$ and $\Phi_{\rm Planck}$.

3.3. CASI-3D Performance on the Full Taurus ^{12}CO and ^{13}CO Map

In this section, we apply our CASI-3D model to the full Taurus ^{12}CO and ^{13}CO map. We compare the CASI-3D predicted magnetic field directions with the dust polarization predicted magnetic field directions.

Figures 8 and 9 show the performance of CASI-3D to predict magnetic field directions on the full Taurus ^{12}CO and ^{13}CO emission data. We also show the magnetic field directions inferred by VGT for comparison. Note that our current CASI-3D model is only trained on sub- and trans-Alfvénic turbulent simulations, which do not include self-gravity. Consequently, if there is self-gravity or other dynamical processes, such as feedback or large-scale converging gas flows, CASI-3D is not able to correctly infer the direction of magnetic fields. However, if CASI-3D predicted magnetic field directions are similar to those inferred by Planck dust polarized emission, it is likely that this region is closer to the trans-Alfvénic regime, indicating relatively strong magnetic field strengths. We highlight some of these regions in red boxes in Figures 8 and 9, where CASI-3D inferred magnetic field direction is very similar to that inferred from Planck dust polarized emission.

To better evaluate the performance of CASI-3D we show the angle difference between the CASI-3D predicted magnetic field directions and those inferred by Planck dust polarized emission in Figures 10 and 11. In most regions, the angle difference

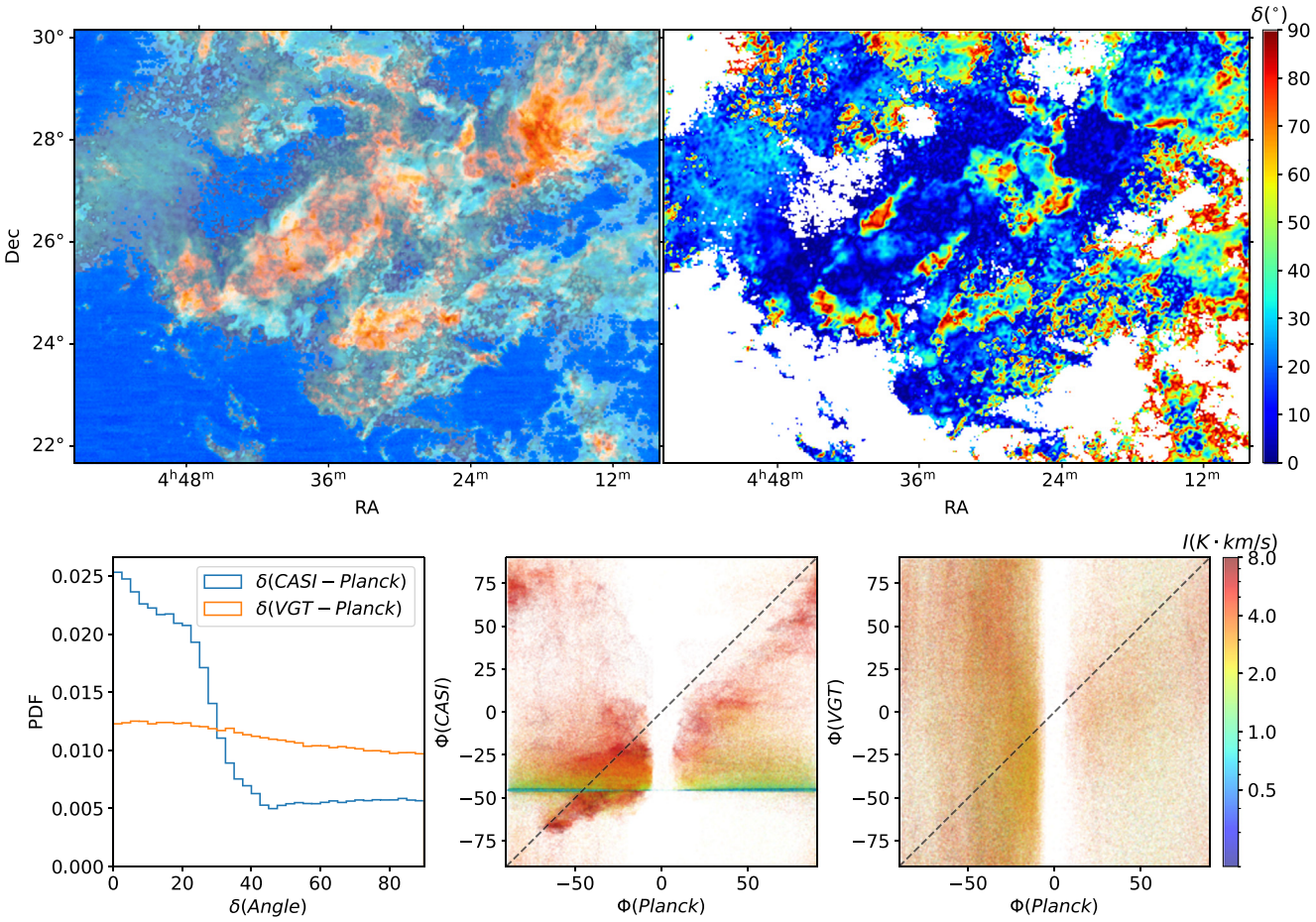

Figure 10. Upper left: integrated ^{12}CO emission overlaid with gray shadows indicating the location where CASI-3D predicted magnetic field directions are similar to those inferred by Planck dust polarized emission. Upper right: angle difference between the CASI-3D predicted magnetic field directions and those inferred by Planck dust polarized emission. Lower left: distribution of the angle difference between the CASI-3D predicted magnetic field directions and those inferred by Planck, and the angle difference between velocity channel gradient (VGT) inferred magnetic field directions and those inferred by Planck. Lower middle: scatter plot between the Planck dust polarization inferred magnetic field directions $\Phi_{\rm Planck}$ and the CASI-3D predicted directions $\Phi_{\rm CASI}$. Lower right: scatter plot between the Planck dust polarization inferred magnetic field directions $\Phi_{\rm Planck}$ and the VGT predicted directions $\Phi_{\rm VGT}$. The color in the scatter plots indicate the integrated intensity of ^{12}CO at each pixel.

Table 2
Statistical Results of the Performance of CASI-3D and VGT

Model	$\mathcal{M}_A$	$\delta_{\rm CASI-3D}$ (°)			$\delta_{\rm VGT}$ (°)		
		Mean	Median	Dispersion	Mean	Median	Dispersion
Turb1	1.24	−6.1	−5.2	15.8	7.6	7.9	28.3
Turb2	0.62	−6.3	−6.2	4.8	14.6	14.2	23.0
Turb3	1.75	18.6	18.4	28.7	13.8	15.3	35.1
Turb4	0.87	−1.8	−1.5	2.8	15.8	15.7	16.1

between the CASI-3D predicted magnetic field directions and those inferred by Planck dust polarized emission, denoted as δ (CASI − Planck), is less than 20°, as shown in the shadowed region in Figures 10 and 11. This indicates that self-gravity is likely not dominant in these regions. On the other hand, in the upper right panel of Figures 10 and 11, we notice that in some regions the magnetic field directions inferred by CASI-3D are dissimilar ($\geqslant$45°), even perpendicular, to those inferred by dust polarization. This is likely caused by self-gravity or large-scale gas flows, where the gas morphology is not particularly regulated by magnetic fields (e.g., Otto et al. 2017; Luk et al. 2022). It is worth noting that not all high column density regions show large differences between CASI-3D predicted magnetic field directions and those inferred by Planck dust polarized emission. As shown in the scatter plots in Figures 10 and 11, a significant amount of pixels with small δ (CASI − Planck) also have strong integrated intensities.

The magnetic field directions inferred by CASI-3D on ^{12}CO and ^{13}CO are mostly consistent, especially in the red boxes in Figures 8 and 9. This demonstrates the robustness of machine learning to handle different molecular emission data. Although ^{12}CO is optically thick near the central velocity channels, CASI-

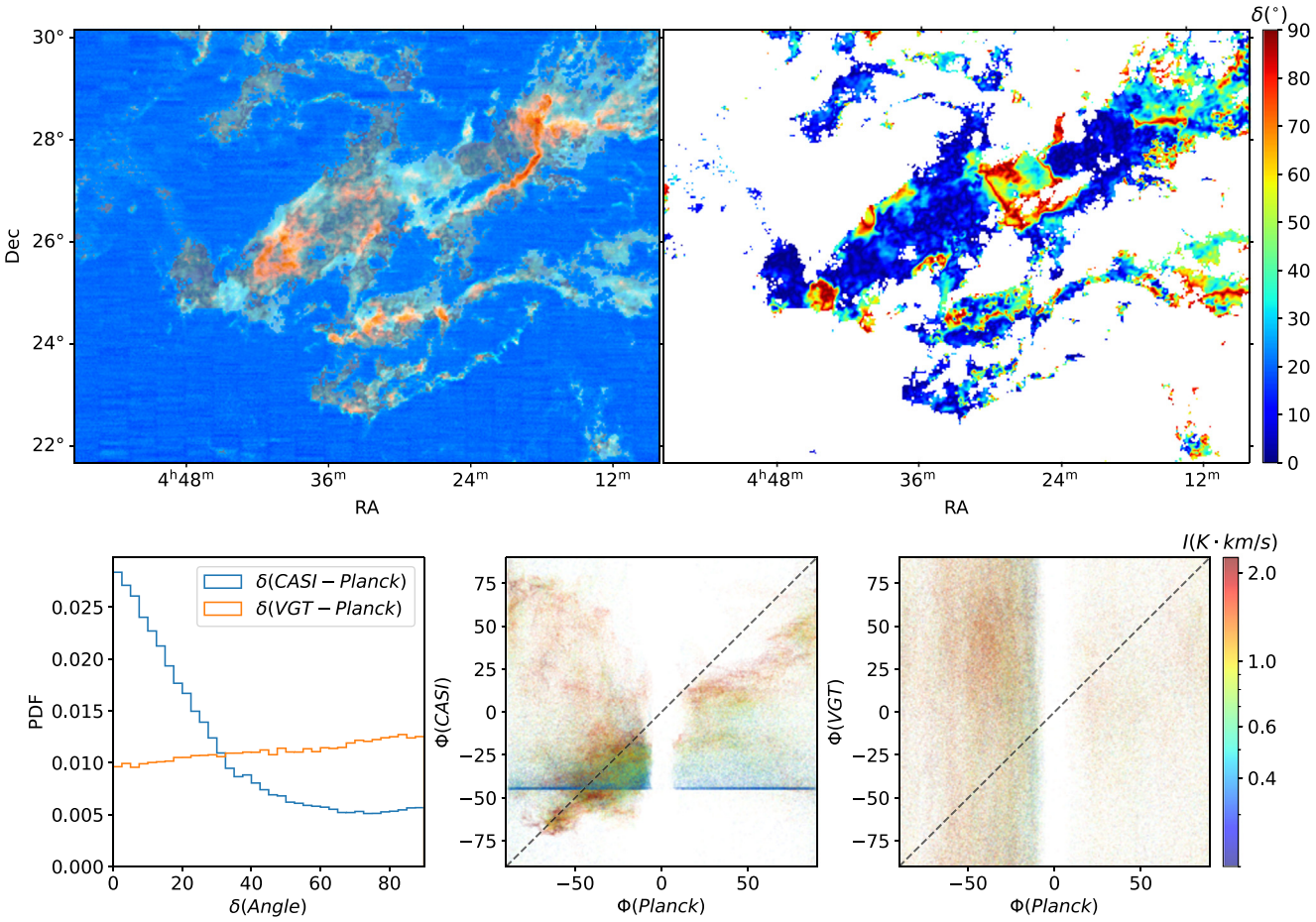

Figure 11. Same as Figure 10, but for ^{13}CO.

3D is still able to capture their morphology to infer the magnetic field directions (however, for discussion of the effect of optical depth, see, e.g., Heyer et al. 2020; Luk et al. 2022). When comparing the magnetic field directions inferred by VGT and that by Planck dust polarized emission, we notice significant fluctuations on small scales. This in turn proves that VGT likely requires large subblock averaging to obtain a robust result. Consequently, it is almost impossible to derive a high-resolution magnetic field map by VGT, but possible by CASI-3D. The current Taurus ^{12}CO and ^{13}CO observation has a pixel resolution of 23″, which is three times higher than that of the Planck dust emission map (1.′07). In the future, we will apply the CASI-3D model to the FUGIN (FOREST Unbiased Galactic plane Imaging survey with the Nobeyama 45 m telescope) project (Umemoto et al. 2017), which will yield maps that are a factor of 9 higher resolution than those from Planck.

4. Conclusions

We have trained the deep learning method CASI-3D to predict the orientation of magnetic fields in sub- and trans-Alfvénic turbulent clouds from molecular line emission. We have tested the CASI-3D performance on synthetic test samples and real observational data. Our main findings are as follows:

1. CASI-3D is able to predict the magnetic field directions from molecular line emission at a pixel level with higher accuracy than that from VGT for sub- and trans-Alfvénic clouds.
2. CASI-3D achieves higher accuracy in sub-Alfvénic clouds ($\lesssim$10°) than that in trans-Alfvénic clouds ($\lesssim$30°). This is consistent with our intuition, where stronger magnetic fields play a more important role in regulating the morphology of clouds.
3. CASI-3D is able to infer the magnetic field direction of a sub-Alfvénic region in Taurus from ^{12}CO emission. The prediction is consistent with the Planck dust polarized emission inferred magnetic field directions, which has a systematical offset of −13° and a dispersion of 9.5°.
4. We have applied CASI-3D to the full Taurus ^{12}CO and ^{13}CO maps, yielding B − field morphology information at a three times higher angular resolution than the Planck-derived map. We find that in many regions CASI-3D inferred magnetic field directions are similar to those inferred from Planck dust polarized emission. This implies that much of the Taurus region is in the sub-Alfvénic regime, i.e., subject to relatively strong, dynamically important magnetic fields.

We thank the anonymous referee for comments that improved this manuscript. D.X. acknowledges support from the Virginia Initiative on Cosmic Origins (VICO). C-Y.L. acknowledges support from an ESO Ph.D. studentship. J.C.T. acknowledges support from NSF grant AST-2009674 and ERC Advanced Grant MSTAR. D.X. thanks Zhi-Yun Li for helpful discussions. The authors acknowledge Research Computing at The University of Virginia for providing computational

resources and technical support that have contributed to the results reported within this publication.

Appendix
Examination of CASI-3D Performance on Different Simulations

In this section, we evaluate the performance of CASI-3D on the synthetic observations of the simulations from Cho & Lazarian (2003) and Burkhart et al. (2009). The simulations adopt a second-order-accurate hybrid essentially nonoscillatory (ENO) scheme (Cho & Lazarian 2002) to solve the ideal MHD equations in a periodic box. The turbulence is driven solenoidally at wave scale k equal to about 2.5, which is different to our simulation in Section 2.1. In our simulations, we drive turbulence with $1 \leqslant k \leqslant 2$, and $\frac{2}{3}$ of the total power is in solenoidal motions and the rest $\frac{1}{3}$ is in compressive motions. This indicates no bias of imposing solenoidal or compressive modes (Dubinski et al. 1995). We adopt the run with $\mathcal{M}_S = 7$ and $\mathcal{M}_A = 0.7$. We assume a kinetic temperature of 20 K, which yields a sound speed of 0.27 km s^{-1} and a turbulent velocity of 1.86 km s^{-1}. We assume a mean density of 523 cm^{-3}, which is the same as our runs. This indicates a mean magnetic field strength of 12 μG. We conduct radiative transfer following exactly the same process as Section 2.2 to generate ^{12}CO and ^{13}CO emission.

Figure 12 shows the performance of CASI-3D to infer the orientation of magnetic fields on the synthetic ^{12}CO data of ENO simulations. We present scatter plots between the true magnetic field directions $\Phi_{\rm True}$ and the predicted ones by CASI-3D $\Phi_{\rm CASI}$, and by VGT $\Phi_{\rm VGT}$ in Figure 13. We also show the channel-by-channel prediction by CASI-3D in Figure 14. To sum up, the dispersion of $\delta_{\rm CASI}$ is 10.°3, which is much smaller than the dispersion of $\delta_{\rm VGT}$, which is 24.°7 on the synthetic ENO data sets. CASI-3D performs robustly in predicting magnetic field directions across different simulations, which provides confidence to apply CASI-3D to other observational data.

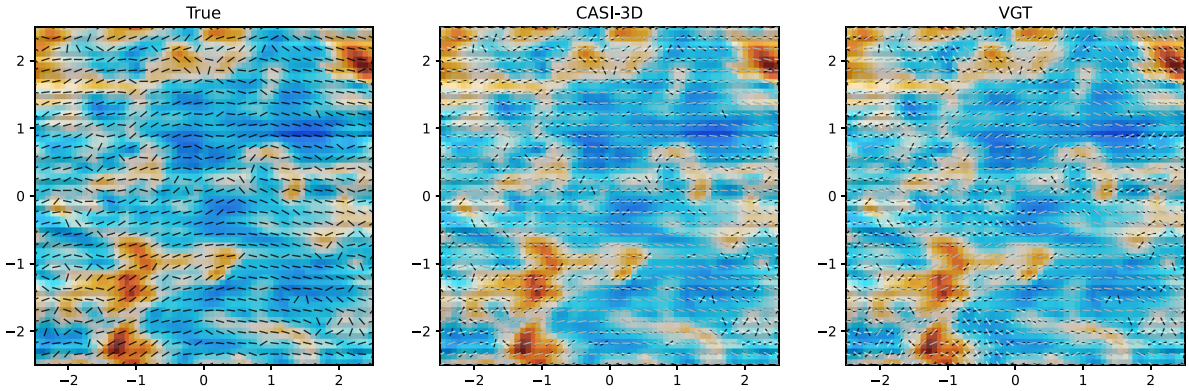

Figure 12. Performance of CASI-3D and VGT to infer the orientation of magnetic fields on the synthetic ^{12}CO data of ENO simulations.

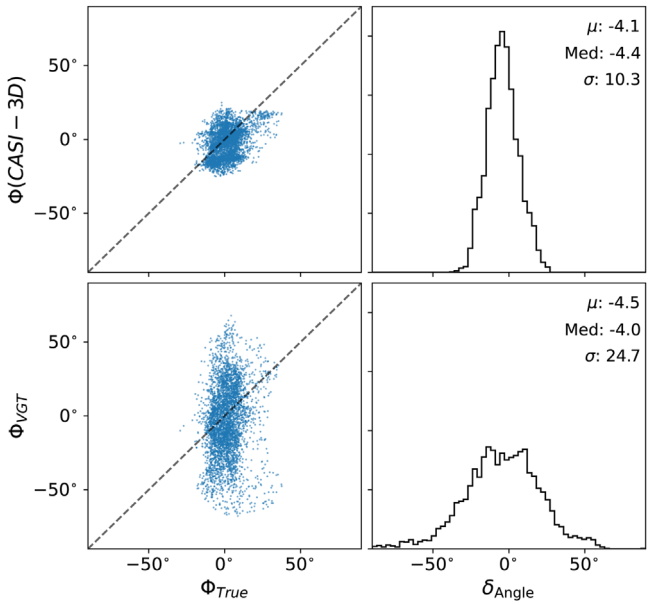

Figure 13. Upper left: scatter plot between the true magnetic field directions $\Phi_{\rm True}$ and the CASI-3D predicted directions $\Phi_{\rm CASI}$ for the synthetic ^{12}CO data of ENO simulations. Lower left: scatter plot between the true magnetic field directions $\Phi_{\rm True}$ and the VGT predicted directions $\Phi_{\rm VGT}$. Upper right: the histogram of the angle difference between $\Phi_{\rm Planck}$ and $\Phi_{\rm CASI}$. Lower right: the histogram of the angle difference between $\Phi_{\rm Planck}$ and $\Phi_{\rm VGT}$.

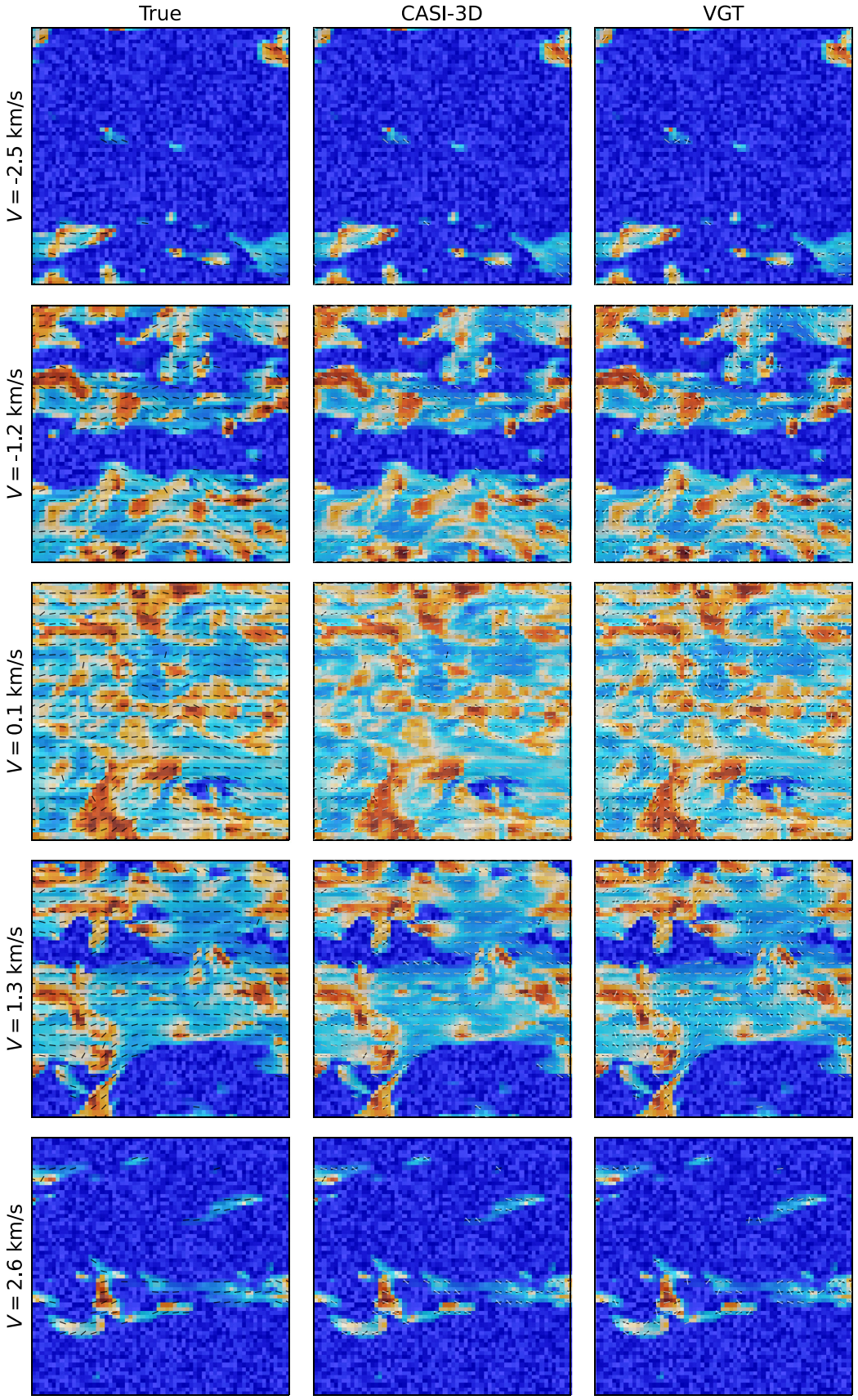

Figure 14. Performance of CASI-3D and VGT to infer the orientation of magnetic fields across multiple velocity channels on the synthetic ^{12}CO data of ENO simulations. The background is the ^{12}CO emission at each velocity channel. The black lines indicate the true POS magnetic field directions at each velocity channel. The gray lines in the middle column indicate the POS magnetic field directions predicted by CASI-3D. The gray lines in the right column indicate the POS magnetic field directions calculated by VGT.

ORCID iDs

Duo Xu https://orcid.org/0000-0001-6216-8931
Chi-Yan Law https://orcid.org/0000-0003-1964-970X
Jonathan C. Tan https://orcid.org/0000-0002-3389-9142

References

Bai, X., Liu, H., Deng, Y., et al. 2021, A&A, 652, A143
Beck, R., & Graeve, R. 1982, A&A, 105, 192
Bisbas, T. G., Papadopoulos, P. P., & Viti, S. 2015, ApJ, 803, 37
Bisbas, T. G., Tan, J. C., & Tanaka, K. E. I. 2021, MNRAS, 502, 2701
Burkhart, B., Falceta-Goncalves, D., Kowal, G., & Lazarian, A. 2009, ApJ, 693, 250
Burn, B. J. 1966, MNRAS, 133, 67
Cho, J., & Lazarian, A. 2002, PhRvL, 88, 245001
Cho, J., & Lazarian, A. 2003, MNRAS, 345, 325
Clark, S. E., Hill, J. C., Peek, J. E. G., Putman, M. E., & Babler, B. L. 2015, PhRvL, 115, 241302
Clark, S. E., Peek, J. E. G., & Miville-Deschênes, M. A. 2019, ApJ, 874, 171
Clark, S. E., Peek, J. E. G., & Putman, M. E. 2014, ApJ, 789, 82
Crutcher, R. M. 1999, ApJ, 520, 706
Crutcher, R. M. 2012, ARA&A, 50, 29
Crutcher, R. M., Wandelt, B., Heiles, C., Falgarone, E., & Troland, T. H. 2010, ApJ, 725, 466
Davis, L. J., & Greenstein, J. L. 1951, ApJ, 114, 206
Dieleman, S., Willett, K. W., & Dambre, J. 2015, MNRAS, 450, 1441
Dubinski, J., Narayan, R., & Phillips, T. G. 1995, ApJ, 448, 226
Dullemond, C. P., Juhasz, A., Pohl, A., et al. 2012, RADMC-3D: A Multi-purpose Radiative Transfer Tool, Astrophysics Source Code Library, ascl:1202.015
Elmegreen, B. G., & Scalo, J. 2004, ARA&A, 42, 211
Federrath, C. 2015, MNRAS, 450, 4035
Fosalba, P., Lazarian, A., Prunet, S., & Tauber, J. A. 2002, ApJ, 564, 762
Goldreich, P., & Sridhar, S. 1995, ApJ, 438, 763
Goldsmith, P. F., Heyer, M., Narayanan, G., et al. 2008, ApJ, 680, 428
González-Casanova, D. F., & Lazarian, A. 2017, ApJ, 835, 41
Grenier, I. A., Casandjian, J.-M., & Terrier, R. 2005, Sci, 307, 1292
Han, J. L. 2017, ARA&A, 55, 111
He, K., Zhang, X., Ren, S., & Sun, J. 2016, in Proc. of the IEEE Conf. on Computer Vision and Pattern Recognition (Piscataway, NJ: IEEE), 770
Heyer, M., Goldsmith, P. F., Yıldız, U. A., et al. 2016, MNRAS, 461, 3918
Heyer, M., Soler, J. D., & Burkhart, B. 2020, MNRAS, 496, 4546
Hoang, T., & Lazarian, A. 2008, MNRAS, 388, 117
Hollenbach, D. J., & Tielens, A. G. G. M. 1999, RvMP, 71, 173
Hu, Y., Yuen, K. H., Lazarian, V., et al. 2019, NatAs, 3, 776
Hutschenreuter, S., Anderson, C. S., Betti, S., et al. 2022, A&A, 657, A43
Inoue, T., & Inutsuka, S.-i. 2016, ApJ, 833, 10
Jansson, R., & Farrar, G. R. 2012, ApJL, 761, L11
Joncas, G., Boulanger, F., & Dewdney, P. E. 1992, ApJ, 397, 165
Lazarian, A., & Vishniac, E. T. 1999, ApJ, 517, 700
Lazarian, A., & Yuen, K. H. 2018, ApJ, 853, 96
Li, H.-b., Dowell, C. D., Goodman, A., Hildebrand, R., & Novak, G. 2009, ApJ, 704, 891
Li, P. S., Martin, D. F., Klein, R. I., & McKee, C. F. 2012, ApJ, 745, 139
Liu, M., Hu, Y., & Lazarian, A. 2022, MNRAS, 510, 4952
Luk, S.-S., Li, H.-b., & Li, D. 2022, ApJ, 928, 132
Mac Low, M.-M. 1999, ApJ, 524, 169
McKee, C. F., & Ostriker, E. C. 2007, ARA&A, 45, 565
Narayanan, G., Heyer, M. H., Brunt, C., et al. 2008, ApJS, 177, 341
Otto, F., Ji, W., & Li, H.-b. 2017, ApJ, 836, 95
Padoan, P., & Nordlund, Å. 1999, ApJ, 526, 279
Pearson, K. A., Palafox, L., & Griffith, C. A. 2018, MNRAS, 474, 478
Peek, J. E. G., & Burkhart, B. 2019, ApJL, 882, L12
Planck Collaboration, Abergel, A., Ade, P. A. R., et al. 2011, A&A, 536, A24
Planck Collaboration, Ade, P. A. R., Aghanim, N., et al. 2016, A&A, 586, A138
Planck Collaboration, Aghanim, N., Akrami, Y., et al. 2020, A&A, 641, A12
Rao, R., Crutcher, R. M., Plambeck, R. L., & Wright, M. C. H. 1998, ApJL, 502, L75
Ridge, N. A., Di Francesco, J., Kirk, H., et al. 2006, AJ, 131, 2921
Ronneberger, O., Fischer, P., & Brox, T. 2015, International Conference on Medical Image Computing and Computer-assisted Intervention (Berlin: Springer), 234
Soler, J. D. 2019, A&A, 629, A96
Soler, J. D., & Hennebelle, P. 2017, A&A, 607, A2
Soler, J. D., Hennebelle, P., Martin, P. G., et al. 2013, ApJ, 774, 128
Soler, J. D., Ade, P. A. R., Angilè, F. E., et al. 2017, A&A, 603, A64
Soler, J. D., Beuther, H., Rugel, M., et al. 2019, A&A, 622, A166
Troland, T. H., & Heiles, C. 1986, ApJ, 301, 339
Umemoto, T., Minamidani, T., Kuno, N., et al. 2017, PASJ, 69, 78
Van Oort, C. M., Xu, D., Offner, S. S. R., & Gutermuth, R. A. 2019, ApJ, 880, 83
Xu, D., Li, D., Yue, N., & Goldsmith, P. F. 2016, ApJ, 819, 22
Xu, D., Offner, S. S. R., Gutermuth, R., Kong, S., & Arce, H. G. 2022, ApJ, 926, 19
Xu, D., Offner, S. S. R., Gutermuth, R., & Oort, C. V. 2020a, ApJ, 890, 64
Xu, D., Offner, S. S. R., Gutermuth, R., & Oort, C. V. 2020b, ApJ, 905, 172
Yuen, K. H., & Lazarian, A. 2017, ApJL, 837, L24
Zhang, Y., Guo, Z., Wang, H. H., & Li, H. b. 2019, ApJ, 871, 98